

Effect of internal geometry and orientation on the performance of a helium-filled soap bubble nozzle

Bradley Gibeau¹, Drew Gingras¹, Jan Raffel¹, Markus Raffel²,
and Sina Ghaemi^{1*}

¹University of Alberta, Department of Mechanical Engineering, Edmonton, Canada

²German Aerospace Center (DLR), Institute of Aerodynamics and Flow Technology, Göttingen, Germany

*ghaemi@ualberta.ca

Abstract

Various design considerations for helium-filled soap bubble generators are investigated. These include the effects of modifying internal nozzle geometry and nozzle operating orientation on nozzle performance, as well as the tracing fidelity of the bubbles produced by a multi-nozzle system and the impact of placing a full-scale generator in the settling chamber of a wind tunnel. Modifications to internal nozzle geometry are found to directly impact the nozzle production regimes, and some evidence is provided to suggest that operating orientation does the same. The mean time responses are found to obey a previously defined theoretical relationship (Engler Faleiros et al. 2019, *Exp Fluids*), and the standard deviations of the time response distributions indicate that 95% of the bubbles produced by the system will accurately track velocity fluctuations with a time scale of 3 ms or greater when the bubbles are neutrally buoyant on average. Placing a full-scale generator in the settling chamber of a wind tunnel is found to increase the maximum freestream deficit by up to 1.2% and the freestream turbulence intensity by at most 0.3% for freestream velocities between 6 and 30 m/s.

1 Introduction

The use of helium-filled soap bubbles (HFSBs) has been explored recently for their potential to allow for particle velocimetry measurements on a larger scale (Scarano et al. 2015). Currently, it is not clear how HFSB nozzles should be designed and operated for optimal performance. Recent investigators (Gibeau and Ghaemi 2018; Engler Faleiros et al. 2018, 2019) utilized different nozzle geometries and operated their nozzles in different orientations, and it is not known how either of these parameters affect nozzle performance. Moreover, the impact of a full-scale generator on the freestream flow quality when placed in a wind tunnel has only been briefly investigated (Jux et al. 2018). The present investigation seeks progress towards answers for these questions.

Three orifice-type nozzles (Bosbach et al. 2009) with different internal geometries are considered here, with one matching the internal geometry used by Gibeau and Ghaemi (2018). All three nozzles were operated vertically pointing downwards, and one was operated horizontally. Shadowgraphy measurements are used to visualize bubble formation and calculate the size distributions of the resulting bubbles. These measurements are used to form maps of the production regimes, mean bubble diameters, and the associated diameter standard deviations. Particle tracking velocimetry (PTV) measurements in a deceleration field are then used to quantify the time response of the bubbles. Finally, planar particle image velocimetry (PIV) and hotwire measurements are used to study the impact of a full-scale HFSB generator on the mean flow quality in a wind tunnel.

2 The nozzles and full-scale HFSB generator

Schematics of the three orifice-type (0.85 mm orifice) nozzles utilized in this study are provided in Figure 1. Nozzle 1 features the same internal geometry used by Gibeau and Ghaemi (2018), and Nozzle 2 and Nozzle 3 are modified versions of the first. The modifications were made to improve air flow within the nozzle to promote the concentricity of the three internal flows. The two primary components of each nozzle, the body and the cap, have been manufactured using a Formlabs 3D printer (Form 2). The remaining parts consist of a sealing o-ring and stainless-steel tubing to provide smooth flow paths for the air, helium (He) and bubble film solution (BFS). More details regarding the nozzle assembly process are provided by Gibeau and Ghaemi (2018).

The full-scale system presented in Figure 2 is an extension of the modular design proposed by Gibeau and Ghaemi (2018). A stand consisting of two NACA 0012 profiles supports customizable ducts in various configurations to allow for tailoring of the shape of the HFSB streamtube. The nozzles are mounted vertically pointing downwards at the top of each duct and can be aligned in series to increase seeding density at a given location in the streamtube plane. Each component of the full-scale structure has been 3D-printed and therefore new ducts can be easily manufactured to accommodate various nozzle configurations.

3 Experiments

Various experiments have been conducted to investigate nozzle operation, bubble diameters, bubble time responses, and the flow quality downstream from the full-scale generator. The former was studied using high-magnification shadowgraphy of the nozzle outputs. An Imager Intense camera featuring a 1376×1040-pixel CCD sensor with a 6.45×6.45 μm^2 pixel size and 12-bit resolution was used to collect images. Illumination was provided by a dual-cavity Nd:YAG laser (New Wave Research, Solo PIV III) capable of producing 532 nm light at 50 mJ per pulse at 15 Hz repetition rate. A diffuser was attached to the output of the laser to obtain diffuse backlight illumination for the experiment. A 12× Navitar zoom lens was used to obtain a resolution of 18.2 $\mu\text{m}/\text{pix}$ in a field of view (FOV) of 15.1×6.4 mm^2 . The volumetric flowrates for air (\dot{V}_{Air}), He (\dot{V}_{He}), and BFS (\dot{V}_{BFS}) were varied in the ranges $0.50 \leq \dot{V}_{\text{Air}} \leq 1.75$ L/min, $0.06 \leq \dot{V}_{\text{He}} \leq 0.26$ L/min, and $7 \leq \dot{V}_{\text{BFS}} \leq 13$ mL/h, respectively, for a total of 144 operating points for each nozzle. A multi-syringe pump (World Precisions Instruments, AL-8000) was used to regulate the flow of BFS, while two 10 L/min digital flow controllers (Cole-Parmer, model # 32907-71) were used to regulate the flows of air and He. Ensembles of 600 double-frame images were collected over a period of 1 minute for each case, resulting in 576 considered operating cases total. The particle sizing feature of DaVis 8.4 (LaVision GmbH) was used to calculate the size distributions of the resulting HFSBs.

The time response of the HFSBs was measured by applying PTV to the bubbles in a

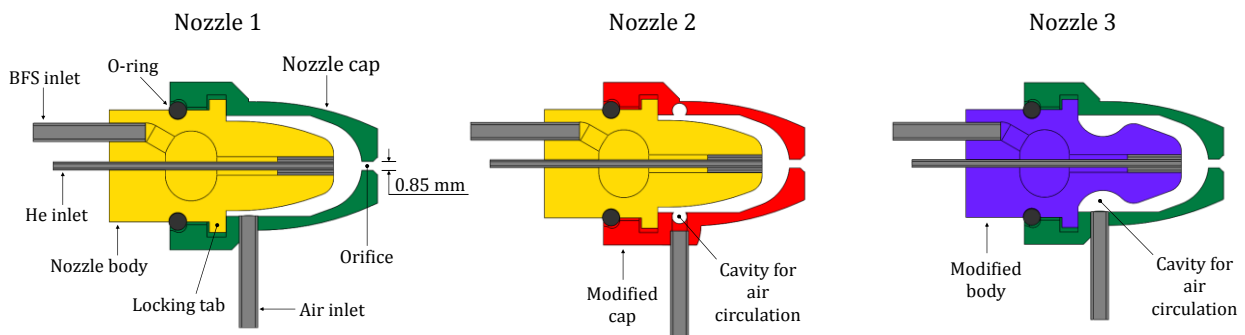


Figure 1. Schematics of the three orifice-type nozzles considered. The schematics are to scale.

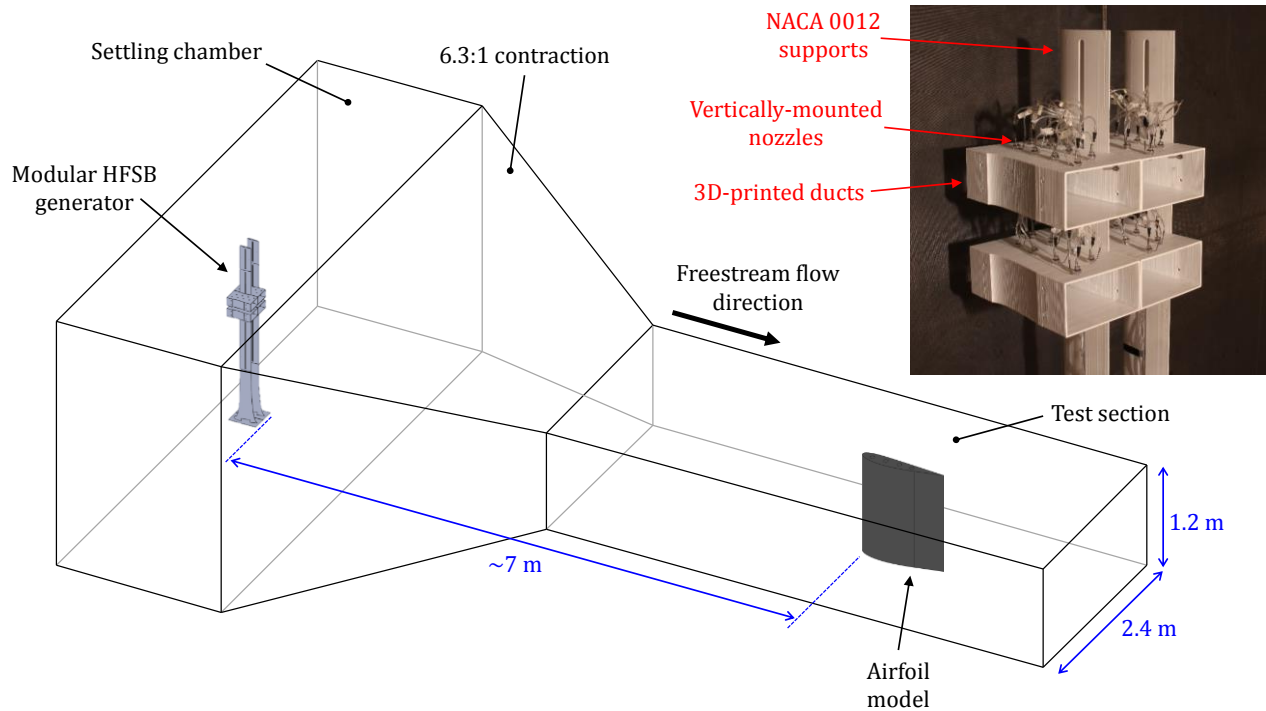


Figure 2. Schematic of the overall full-scale setup. The top right photograph shows the present modular HFSB generator, which has been 3D printed.

deceleration field leading up to a stagnation point. The deceleration in the experiment was induced by a NACA 4418 airfoil at zero angle of attack as shown in Figure 2. One module was used along with 8 nozzles for these experiments. The same multi-syringe pump and digital flow controller used for shadowgraphy were used to regulate the flows of BFS and He, respectively. A 50 L/min digital flow controller (Omega, model # FMA-LP2609A) was used to regulate the larger flowrates of air required for 8 nozzles. A Phantom v611 high-speed camera featuring a 1280×800-pixel CMOS sensor with a 20×20 μm² pixel size and 12-bit resolution was used to take time-resolved images of the HFSBs for particle tracking. Illumination was provided by a dual-cavity Nd:YLF laser (Photonics Industries, DM20-527-DH) capable of producing 527 nm light at 20 mJ per pulse at 1 kHz repetition rate. Higher repetition rates are possible at lower energy per pulse. Several optics were used to form a horizontal laser sheet with a 2-mm thickness located 30 cm from the wind tunnel floor just upstream from the leading edge of the airfoil. A 50-mm Nikon lens with an aperture setting of $f/4$ was used to obtain a cropped FOV of 196×196 mm² with a resolution of 245 μm/pix. The larger FOV was used to eliminate the doublet patterns produced by the large HFSBs, which interfere with particle tracking. All time response experiments were conducted at a freestream velocity of 12.3 m/s. A set of 3900 double-frame images was recorded using standard 1-μm particles that were generated using a fog machine. This data forms the reference set to which all HFSB tracks will be compared. Sets of 7800 single-frame images were recorded at an acquisition frequency of 6 kHz for the considered HFSB cases. DaVis 8.4 was used to process the images. The reference set was preprocessed by subtracting the ensemble minimum and then normalizing with the ensemble average. A sum-of-correlation algorithm (Meinhart et al. 2000) was then applied using 24×24-pixel (5.9×5.9-mm) Gaussian interrogation windows with 75% overlap to obtain the reference mean velocity field. The time-resolved sets were processed using the DaVis 2D-PTV algorithm to obtain individual bubble tracks. Bubbles were detected using a Gaussian 3×3 fit with a minimum intensity threshold of 250 counts. All tracks with lengths of less than 11 time steps were discarded.

The times responses (τ) were calculated as the ratio of slip velocity and bubble acceleration (Scarano et al. 2015):

$$\tau = \frac{\vec{U}_{\text{ref}} - \vec{U}_{\text{HFSB}}}{\vec{a}_{\text{HFSB}}} \quad (1)$$

where the numerator, i.e. the slip velocity, is the difference between the reference velocity and the velocity of a HFSB, and the denominator is the acceleration of the same HFSB. The reference velocity at a given point has been obtained by linearly interpolating the reference velocity field, while the velocity and acceleration of each HFSB has been obtained by fitting a second-order polynomial to the bubble locations obtained from PTV using a least-squares method. Eq. (1) was applied to all PTV tracks in a $30 \times 30 \text{ mm}^2$ region beginning 5 mm upstream from the front stagnation point of the airfoil for each considered case.

The flow quality downstream from the modular HFSB generator ($\sim 5 \text{ m}$ from the end of the contraction) was measured to investigate the effect of the structure on the flow. First, the impact of the modular structure on the mean freestream flow was investigated using planar PIV. The same camera and laser system used for PTV was employed, but two cameras were implemented here to obtain a wider FOV for capturing more of the spanwise direction in the test section. A laser sheet was formed parallel to the wind tunnel floor in the path of the HFSB streamtube with a thickness that varied from 1 to 2 mm due to divergence of the laser over the large FOV. Two 50-mm lenses with aperture settings of $f/5.6$ were used to obtain a stitched FOV of $590 \times 197 \text{ mm}^2$ (spanwise-streamwise) with a resolution of $246 \text{ }\mu\text{m}/\text{pix}$. Sets of 2000 double-frame images were collected at 200 Hz for ten freestream velocities ranging from 3 to 30 m/s, both with and without the modular HFSB generator in the settling chamber of the wind tunnel. DaVis 8.4 was again used to process the images. The image sets were preprocessed by subtracting the ensemble minimums and then normalizing with the ensemble averages. A sum-of-correlation algorithm (Meinhart et al. 2000) was applied using 128×128 -pixel (31.5×31.5 -mm) Gaussian interrogation windows with 75% overlap to obtain mean velocity fields. The freestream turbulence intensity was measured in the path of the streamtube using a hotwire probe (Custom Hot Wires). Velocity measurements at 20 kHz were recorded over 10 seconds for the same range of freestream velocities mentioned above, with and without the modular structure in the settling chamber of the wind tunnel. The mean velocity fields from PIV were used to calibrate the hotwire probe by fitting a least-squares third-order polynomial to the hotwire voltage signals. The turbulence intensity of the freestream flow was then calculated as the root-mean-square of the fluctuating component of velocity divided by the mean.

4 Results

4.1 Nozzle production maps

Engler Faleiros et al. (2019) identified numerous production regimes that orifice-type nozzles can operate within. The two primary categories are bubbling and jetting, and there are subcategories within each. Bubbling refers to when bubbles are produced within the nozzle itself, while jetting refers to bubble production that is external to the nozzle via a jet of He and BFS. Bubble production in each regime is further subcategorized by whether the resulting bubbles are monodisperse or polydisperse. Several non-ideal production regimes are also possible. Satellite bubble formation occurs when two distinct populations of bubbles with different diameters are produced. Merging is when bubbles combine into merged pairs shortly after formation. These production regimes can be problematic because they result in undesirable bubble geometry or highly bimodal bubble distributions, both of which are not ideal for flow measurement. Sample shadow visualizations of the various production regimes observed in the present experiments are shown in Figure 3.

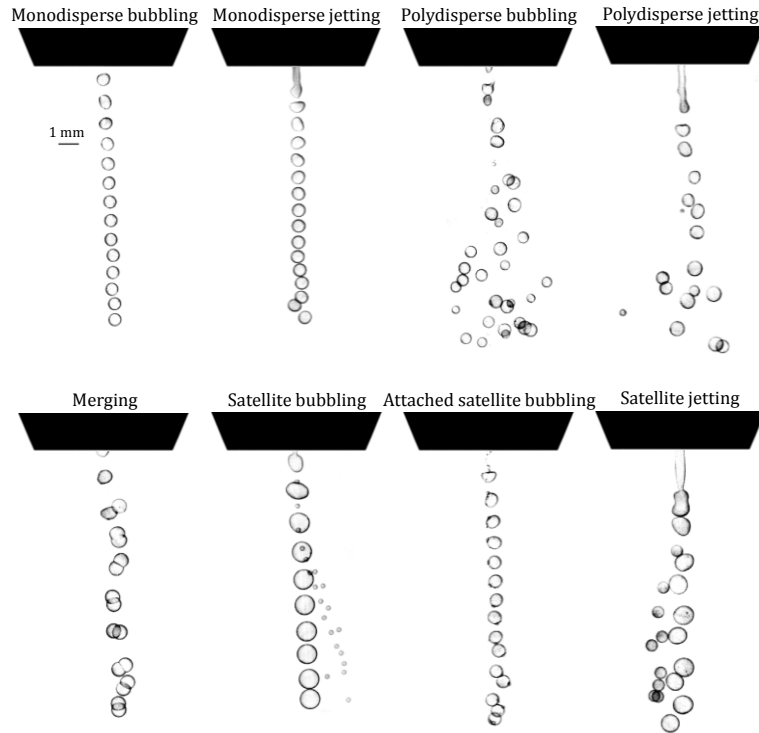


Figure 3. Shadow visualizations of the various production regimes observed using the present nozzles.

Four umbrella production regimes are defined here to further study nozzle performance using production maps following the work of Engler Faleiros et al. (2019). Bubbling will be used to refer to monodisperse, polydisperse, and attached satellite bubbling. Jetting will be used to refer to monodisperse and polydisperse jetting. Transitional refers to operation that intermittently changes between bubbling and jetting. Finally, atypical production will refer to merging, satellite bubbling and jetting, or any operation that switches between one or more of these non-ideal production regimes. Note that attached satellite bubbling is not considered atypical because the bubbles are still highly spherical and monodisperse (see Figure 3).

Qualitative production maps have been formed using the above umbrella regimes for the considered cases: vertical operation of Nozzle 1, Nozzle 2, and Nozzle 3, and horizontal operation of Nozzle 3. These maps are visible in Figure 4, where no attempt to interpolate or form contours of the results has been made to maintain the actual resolution of the maps. First considering vertical operation, it is evident that increasing \dot{V}_{BFS} into each nozzle decreases the tendency for the nozzle to operate in the jetting regime. This effect is significantly more pronounced for Nozzle 2 and Nozzle 3. These two nozzles also experience an increase in the ability to operate in the bubbling regime and a decrease in the ability to operate at higher air input rates when \dot{V}_{BFS} is increased. These trends are accompanied by a movement of the bubbling-jetting transition front to the right on the maps, i.e. in the direction of increasing \dot{V}_{He} . This trend is not visible for Nozzle 1, the map for which appears relatively static with increasing \dot{V}_{BFS} . For all three nozzles, low \dot{V}_{Air} and \dot{V}_{He} (the bottom left corner of each map) are associated with operating in the bubbling regime, while high \dot{V}_{Air} and \dot{V}_{He} (the top right corner of each map) are associated with the jetting regime. Moreover, high \dot{V}_{BFS} is associated with an increase in atypical bubble production in general. Nozzle 3 seems to perform the best overall, as it exhibits bubbling behaviour over the largest range of input combinations. Considering horizontal operation, it is evident that the nozzle does not perform well because stable operation was not achievable for most of the operating points. The ill operation seems to be associated with BFS buildup within the nozzle, and this is corroborated by the fact that the worst performance is

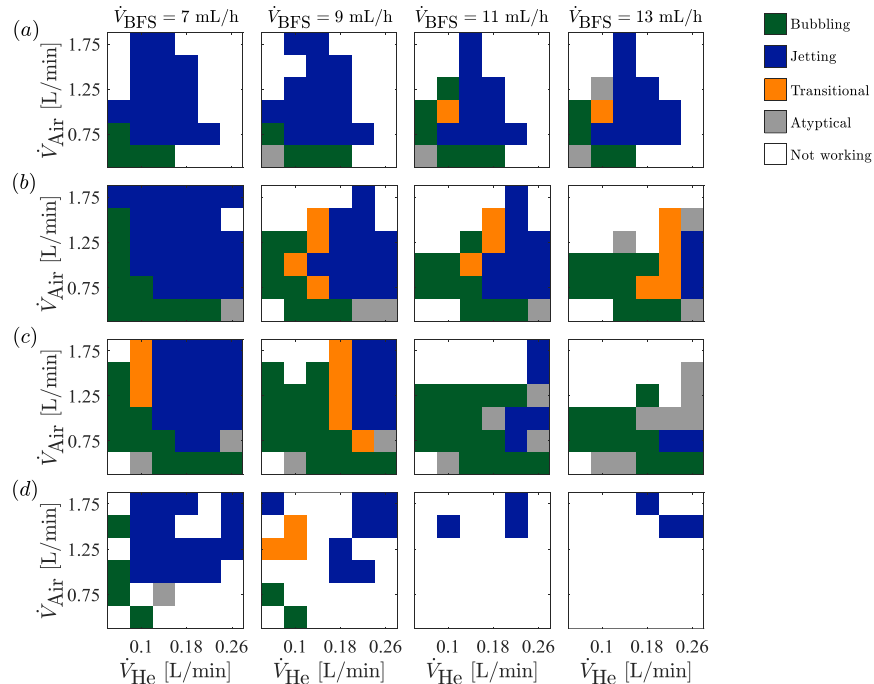


Figure 4. Production maps for (a) Nozzle 1, (b) Nozzle 2, (c) Nozzle 3, and (d) Nozzle 3, horizontal.

observed at high \dot{V}_{BFS} . However, the bubbling-jetting transition front shifts between vertical and horizontal operation, suggesting that nozzle orientation can alter nozzle performance. Only vertical nozzle operation will be considered for the remainder of the discussion.

4.2 Bubble size distributions

The distribution of bubble sizes has been determined for all operating points that exhibit bubbling, jetting, or transitional behaviour. The resulting means and standard deviations have been plotted as maps in Figure 5, where the bubbling regions are outlined in black. Only the first three BFS flowrates are shown for brevity. The maps of mean diameter reveal similar bubble sizes for the same inputs of air and He, i.e. changing internal geometry or the flow of BFS does not have a large impact on mean diameter. In the same regard, whether the nozzle is bubbling, jetting, or transitioning also does not significantly impact mean diameter. In general, increasing \dot{V}_{He} leads to larger bubbles, while increasing \dot{V}_{Air} leads to smaller bubbles. Mean diameters ranging from roughly 0.2 mm to 0.9 mm were found.

While the production regime does not have a large impact on mean diameter, it directly affects the standard deviations of the resulting bubble distributions. As is evident in Figure 5, the bubbles formed in the bubbling regime (black outline) generally have a standard deviation that is less than 5% of the mean. The few exceptions occur for the cases of polydisperse bubbling, which are rare. In contrast, the jetting regime produces bubble distributions with standard deviations that extend upwards of 30% of the mean. The highest standard deviations are found for jetting cases with low \dot{V}_{Air} and high \dot{V}_{He} . The jetting cases with a small standard deviation only occur for monodisperse jetting, which is also rare. The transitional cases result in standard deviations that are roughly 10-20% of the mean and depend on the relative switching between bubbling and jetting.

4.3 Time response distributions

Engler Faleiros et al. (2019) used theory and experiments to show that the mean time response $\bar{\tau}$ varies linearly with the ratio $\dot{V}_{He}/\dot{V}_{BFS}$. This relationship is shown for 24 selected bubbling cases

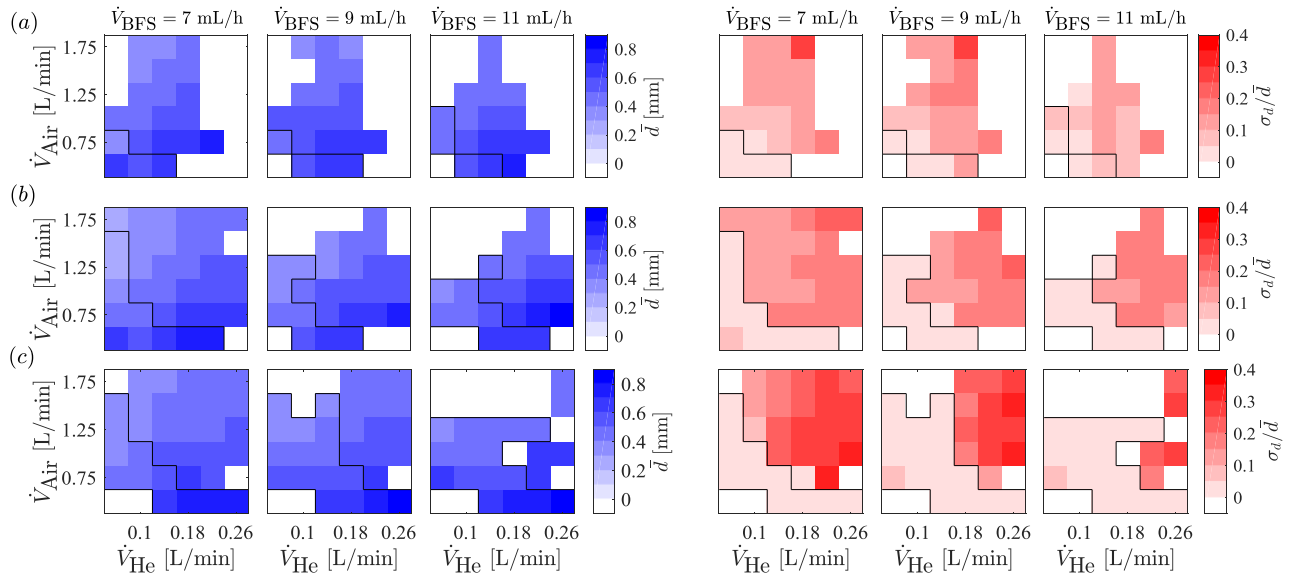


Figure 5. (left) Maps of mean bubble diameter and (right) normalized standard deviations for (a) Nozzle 1, (b) Nozzle 2, and (c) Nozzle 3. The bubbling regions have been outlined in black.

(Nozzle 3) in Figure 6, where the linear relationship is seen to be satisfied. The grey dashed lines in the figure show the point at which this linear relationship should cross $\bar{\tau} = 0$ for the ideal case of no BFS spillage or He leakage ($\dot{V}_{\text{He}}/\dot{V}_{\text{BFS}} \approx 1080$). The present linear relationship falls short to a value of roughly $\dot{V}_{\text{He}}/\dot{V}_{\text{BFS}} = 750$, indicating that soap is spilled during the bubble formation process (Engler Faleiros et al. 2019). Regardless, operating the present HFSB generator using this input ratio will result in bubbles that are approximately neutrally buoyant on average.

The standard deviation of a time response distribution reveals the range of tracing performance that can be expected from the resulting bubbles. These values are plotted as a function of $\dot{V}_{\text{He}}/\dot{V}_{\text{BFS}}$ in Figure 6. The plot reveals a relatively constant standard deviation of roughly $\sigma_{\tau} = 150 \mu\text{s}$ for all cases, although lower values of $\dot{V}_{\text{He}}/\dot{V}_{\text{BFS}}$ show more variance. These values are larger than those reported by Engler Faleiros et al. (2018, 2019), and this is likely due to the multi-nozzle, full-scale system that was utilized here, as opposed to the single nozzle used in their studies. The multi-nozzle system may increase deviation because each nozzle can be slightly different, and it is difficult to ensure an equal distribution of inputs to each. Despite the larger standard deviation of time responses measured here, the present system remains viable for large-scale measurements. Considering that 95% of the bubbles produced by the system will have time responses within two

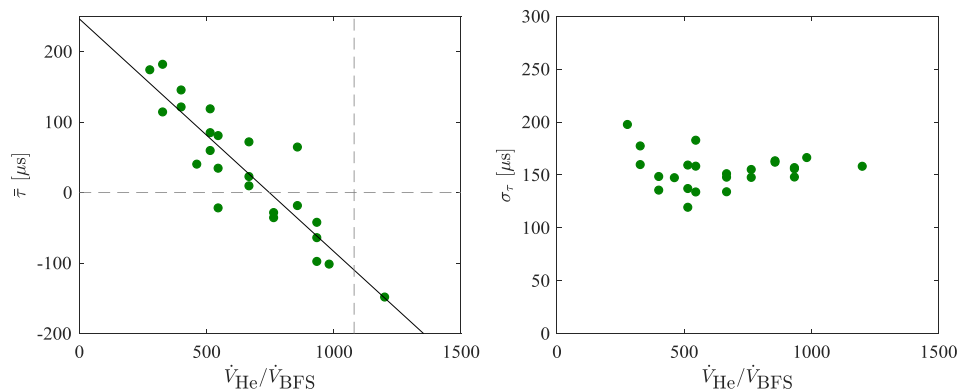


Figure 6. (left) Means and (right) standard deviations of time response as a function of the input parameters.

standard deviations of the mean (normally distributed), the largest values will be roughly $\tau = \pm 300 \mu\text{s}$ for a distribution that is neutrally buoyant on average ($\dot{V}_{\text{He}}/\dot{V}_{\text{BFS}} = 750$). These bubbles will accurately trace flows with a characteristic time scale that is an order of magnitude larger than their time response (Tropea et al. 2007), and therefore velocity fluctuations with a time scale of 3 ms or greater can be measured with negligible error using the present system.

4.4 Full-scale implementation

It is important to consider how using the full-scale HFSB generator in the settling chamber of the wind tunnel affects the downstream flow quality. The velocity deficit caused by the large structure has been quantified using the maximum deviation from the mean freestream velocity. These deviations are plotted in Figure 7 for ten freestream velocities ranging from 3 to 30 m/s. The plot reveals that the largest deviation from the mean without the structure is 1.1% and occurs at the lowest velocity. This larger deviation is due to poor flow quality at low freestream velocities. At 6 m/s or higher, the maximum deviation is 0.7%. This maximum deviation increases to 1.9% when the HFSB structure is added to the settling chamber, revealing that the deficit is increased by at most 1.2% for the considered freestream velocities. As is evident from Figure 7, the largest deviations from the mean occur in the mid-range of velocities studied (~ 10 -20 m/s), and the structure does not seem to impose a noticeable deficit at the highest velocities considered. Figure 7 also shows freestream turbulence intensities for the same cases, which can be seen to follow a similar trend, i.e. poor flow quality at 3 m/s, no affect at the highest velocities, and a maximum impact in the mid-range of velocities. Without the HFSB structure, all freestream turbulence intensities are 0.6% or lower. The freestream turbulence intensity at 6 m/s or higher increases by at most 0.3% when the HFSB structure is added.

The modular HFSB system has been scaled up to the 4-module system shown in Figure 2. A total of 48 nozzles (Nozzle 3) were used to seed the flow in the wake of an Ahmed body for a PTV measurement. A sample image from the experiment is shown in Figure 8. A total volume of approximately 15,000 cm³ was seeded continuously at 10 m/s, resulting in 0.02 particles per pixel.

5 Conclusion

This work investigated several aspects of the utilization of HFSB generators. First, three different internal nozzle geometries were considered. The second and third nozzles were modified versions

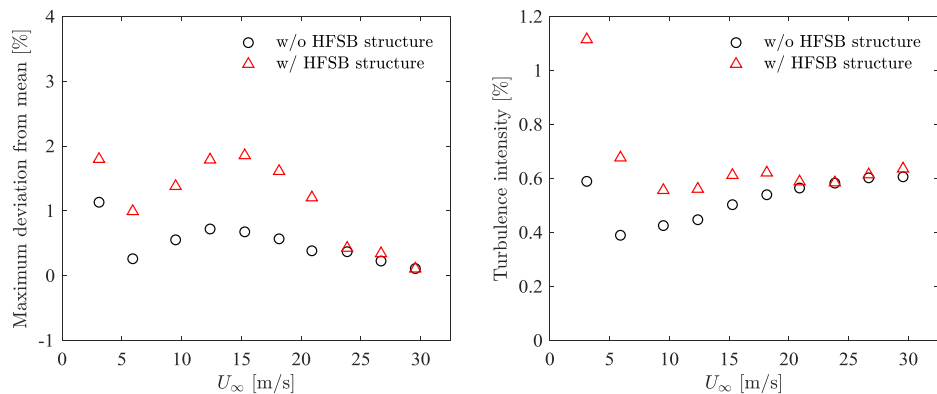


Figure 7. (left) Maximum freestream deviation from the mean and (right) turbulence intensities with and without the HFSB generator in the settling chamber of the wind tunnel.



Figure 8. Inverted sample image showing HFSB seeding in the wake of an Ahmed body with a 19.5×14.4 cm² back face. The experiment was conducted at 10 m/s using 48 nozzles. A volume of roughly 15,000 cm³ is illuminated in the image.

of the first, which is the same geometry used by Gibeau and Ghaemi (2018). The modifications were made to improve air flow in the nozzles to promote the concentricity of the internal flows. It was found that the changes in internal geometry do not significantly affect the mean diameter of the resulting bubbles. However, the geometry directly affects the production regimes of the nozzles for a given combination of input flowrates, which in turn affect the standard deviations of the resulting bubble diameter distributions. Some evidence that operating orientation impacts these production regimes was also found, as the production map of the third nozzle shifted when the nozzle was moved from vertical to horizontal operation. The third nozzle was found to perform the best, as it exhibited desirable bubble production over the largest combination of input parameters. An investigation of the time responses of the bubbles produced by the third nozzle revealed that the mean time response varies linearly with $\dot{V}_{\text{He}}/\dot{V}_{\text{BFS}}$, and this agrees with the theoretical relation derived by Engler Faleiros et al. (2019). This linear relation also revealed that soap is likely spilled during production in the bubbling regime. The standard deviation of the associated time response distributions was found to be relatively constant at 150 μs , revealing that 95% of the bubbles produced by the system will trace velocity fluctuations with a time scale of 3 ms or greater with negligible error when the bubbles are made neutrally buoyant on average. Finally, a full-scale HFSB generator was scrutinized. It was shown that the maximum freestream deficit in the wind tunnel increased from 0.7% to 1.9% when the HFSB generator is added to the settling chamber for freestream velocities between 6 and 30 m/s. This deficit was accompanied by a maximum increase in freestream turbulence intensity of 0.3%. A sample image from an experiment at 10 m/s using 48 nozzles was also provided, showing an illuminated volume of approximately 15,000 cm³ in the wake of an Ahmed body model.

Acknowledgements

We acknowledge the financial support of the Natural Sciences and Engineering Research Council of Canada (NSERC) [Alexander Graham Bell Canada Graduate Scholarship – Doctoral]. We also thank Prof. David Wood of the University of Calgary for lending the hotwire system.

References

- Bosbach J, Kühn M, and Wagner C (2009) Large scale particle image velocimetry with helium filled soap bubbles. *Experiments in Fluids* 46:539-547
- Engler Faleiros D, Tuinstra M, Sciacchitano A, and Scarano F (2018) Helium-filled soap bubbles tracing fidelity in wall-bounded turbulence. *Experiments in Fluids* 59:56
- Engler Faleiros D, Tuinstra M, Sciacchitano A, and Scarano F (2019) Generation and control of helium-filled soap bubbles for PIV. *Experiments in Fluids* 60:40
- Gibeau B and Ghaemi S (2018) A modular, 3D-printed helium-filled soap bubble generator for large-scale volumetric flow measurements. *Experiments in Fluids* 59:178
- Jux C, Sciacchitano A, Schneiders JFG, and Scarano F (2018) Robotic volumetric PIV of a full-scale cyclist. *Experiments in Fluids* 59:74
- Meinhart CD, Wereley ST, and Santiago JG (2000) A PIV algorithm for estimating time-averaged velocity fields. *Journal of Fluids Engineering* 122:285-289
- Scarano F, Ghaemi S, Caridi GCA, Bosbach J, Dierksheide U, and Sciacchitano A (2015) On the use of helium-filled soap bubbles for large-scale tomographic PIV in wind tunnel experiments. *Experiments in Fluids* 56:42
- Tropea C, Yarin AL, and Foss J (2007) Handbook of experimental fluid mechanics. Springer, Berlin